applied sciences

MDPI

*Article*

# Spectral Characteristics of Fluctuating Aerodynamic Forces Acting on Rectangular Prisms

**Jiadong Zeng [1], Zhitian Zhang [1,*], Mingshui Li [2] and Shaopeng Li [3]**

1 College of Civil Engineering and Architecture, Hainan University, Haikou 570228, China; 993757@hainanu.edu.cn
2 Key Laboratory for Wind Engineering of Sichuan Province, Southwest Jiaotong University, Chengdu 610032, China; lms_rcwe@126.com
3 School of Civil Engineering, Chongqing University, Chongqing 400044, China; lishaopeng0314@163.com
* Correspondence: zhangzhitian@hainanu.edu.cn; Tel.: +86-0898-66279232

**Featured Application: A normalized across-wind fluctuating wind load spectrum model is proposed, taking into account the effects of incoming turbulence, the side ratio, vortex shedding, and separation reattachment flow-induced spectral bandwidth changes and high-frequency fluctuations.**

**Abstract:** The present work is devoted to the role of boundary layer turbulence on the spectral characteristics of fluctuating wind loads on large aspect-ratio rectangular prisms. Seven rectangular rigid models with different side ratios (1/4~4) were created, and simultaneous pressure experiments were conducted under the boundary layer turbulence flows. Using the measured data, the power spectrums of the fluctuating aerodynamic forces were calculated, and then, the spectral characteristics under different turbulent boundary layer flows were analyzed. In contrast to the typical power spectrum model, the main factors affecting the spectral characteristics of the fluctuating aerodynamic loads are presented and discussed in this study. The power spectrum of the rectangular prism was significantly impacted by the turbulent wind field, primarily because higher turbulence intensity levels result in a lower spectral peak and a wider spectral bandwidth, which also redistributes spectral energy. In particular, the effect on the spectral properties of across-wind fluctuating loads was stronger, and the turbulent disturbance modified the lateral separation flow structure, causing the reattachment phenomenon to occur earlier on rectangular prisms with small side ratios, which effectively altered the spectral properties. Thus, a normalized across-wind fluctuating wind load spectrum model is proposed, taking into account the effects of incoming turbulence, the side ratio, vortex shedding, separation reattachment flow-induced spectral bandwidth changes, and high-frequency fluctuations.

**Keywords:** fluctuating aerodynamic forces; spectral characteristics; rectangular prism; wind tunnel test

check for updates

**Citation:** Zeng, J.; Zhang, Z.; Li, M.; Li, S. Spectral Characteristics of Fluctuating Aerodynamic Forces Acting on Rectangular Prisms. *Appl. Sci.* **2023**, *13*, 11975. https://doi.org/10.3390/app132111975

Academic Editor: Wei Huang

Received: 21 March 2023
Revised: 21 October 2023
Accepted: 29 October 2023
Published: 2 November 2023



## 1. Introduction

In structural wind engineering, the precise calculation of wind loads acting on structures is a challenging and timely topic of significant interest [1–4]. The boundary layer shear flow across the building surface produces significant three-dimensional flow effects, which can be categorized into along-wind, across-wind, and torsional wind effects [5,6]. An in-depth understanding of fluctuating aerodynamic forces, and the acquisition of an appropriate power spectrum model, are essential when conducting relevant studies so that we may effectively forecast the wind-induced reaction caused by various wind effects [6–9]. However, the non-linear vertical gradient variation of the boundary layer's turbulence parameters causes spectral characteristics in fluctuating wind loads that are challenging to describe using straightforward mathematical formulas [10–12]. This is because of the complicated spatial distribution of the boundary layer's turbulence parameters [13]. Wind loads are evolving into a design control element, and in-depth investigations of wind effects are especially crucial given the current prevalence of 'super tall' building developments. Therefore, thorough research using efficient research techniques is required to understand the spectral characteristics of fluctuating aerodynamic forces on high-rise buildings with large aspect ratios.

It is now generally accepted that along-wind fluctuating wind loads are generally straightforward and mainly determined by the along-wind turbulence component [1,3,5,14]. Davenport [15] created and improved the calculation method for along-wind loads and wind-induced responses, based on the quasi-constant theory and strip assumption; they produced the influential gust factor method that served as the theoretical framework for later studies. The gust load factor approach, or a variant of it, can be utilized to precisely determine the wind-induced response and equivalent static wind load of a building based on the Davenport wind vibration theory [16,17]. Overall, it can be argued that the spectrum properties of along-wind fluctuating loads are mostly compatible with the along-wind fluctuating velocity component, and studies in this area are generally well established.

As a 'super tall' building's height increases, the across-wind loads and wind-induced response frequently outweigh the along-wind direction, and they take control of the structure's design [3,6,7,9,18–20]. The more complicated, across-wind loading, aerodynamic mechanism is primarily affected by a confluence of vortex shedding, separation and reattachment flow, incoming turbulence, and aeroelastic excitation [7–9,20,21]. The applied aerodynamic forces caused by incoming turbulence and wake excitation, and the self-excited forces caused by the structure's air-bounce effect, comprise the two halves of the across-wind load [3,6,7,11,18–22]. Currently, rigid model pressure measurements, base high-frequency dynamic balance force testing, or fluid numerical computations are the main methods used to examine the across-wind fluctuation pressure spectral properties [9,11,19,20,23]. The across-wind fluctuating load spectrum and the basal bending moment spectrum were obtained experimentally by Liang [6], Lin [19], Gu [10], and Quan [20]. They compared and analyzed the effects of wind field type, aspect ratio, and side ratio on power spectrum characteristics in the across-wind and torsional directions. Based on these findings, a number of closed formulas for the power spectrum were developed by fitting the experimental data [3,7,9,16,24,25]. These formulas took into account variables such as the turbulence intensity, turbulence integration scale, vortex shedding frequency, and geometrical characteristic dimensions of the structure. The findings of the aforementioned studies are extremely valuable from an engineering perspective, as they assist with the precise estimation of across-wind loads and wind-induced reactions in high-rise structures. However, it should not be forgotten that the majority of the available spectrum models have some presumptions and prerequisites; this is because their application is limited by an insufficient understanding of boundary layer turbulence, fluid-solid interactions, and spectral features. Additionally, research is frequently conducted using wind tunnel testing, field measurements, or random vibration theory due to the complexity of the torque wind effect's mechanism, although pertinent research findings are rarely reported [26,27].

There are still comparatively few in-depth studies on the mechanistic background of the spectral properties and fluid–solid interactions of fluctuating aerodynamic forces that are subjected to boundary layer turbulence, despite the fact that a great deal of work has been conducted in order to obtain power spectrum models that may be applied to different structural forms. Given that the rectangular cross-section is commonly used for high-rise buildings [8,20,23,28–30], this study developed a group of prismatic building models with side ratios of 1/4 to 4 for wind tunnel testing; this helped to expand our understanding of the aerodynamic spectral characteristics of rectangular prisms. The synchronization pressure measuring technique was used to measure the unsteady surface wind pressures acting on rectangular models. We analyzed the impacts of entering turbulence, the side ratio, vortex shedding, separation reattachment flow-induced spectral bandwidth variations, and high-frequency fluctuations on the spectrum features of the fluctuating aerodynamic forces. A normalized empirical formula for the across-wind fluctuating load power spectrum is suggested, based on the findings of the present study, followed by an examination of the applicability of the conventional power spectrum models.

## 2. Experimental Setup

The experiments were conducted in a closed-circuit wind tunnel, with a test section of 22.5 m (width) × 4.5 m (height) × 36 m (length), as shown in Figure 1. The models were designed to be rigid, and the height of all the models was 1.6 m. The narrow sides of all models were of an identical width, at 100 mm, and the lengths of the other sides varied between 100 mm, 200 mm, 300 mm, and 400 mm, respectively. Therefore, with the 4 models positioned at wind directions of 0° and 90°, one comprised rectangular prisms with seven different side ratios in total (i.e., $D/B$ = 1/4, 1/3, 1/2, 1, 2, 3, and 4). The models were made of transparent Perspex with severed transverse ribs to increase its stiffness. A total of 336 pressure taps were installed on the square model, and 624 pressure taps were installed on each rectangular model. The taps were uniformly distributed across 12 levels (Nos. 1# to 12#), as illustrated in Figure 2.

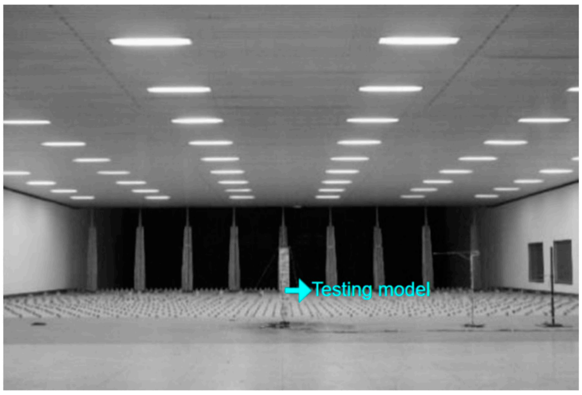


**Figure 1.** A rectangular prism installed in wind tunnel.

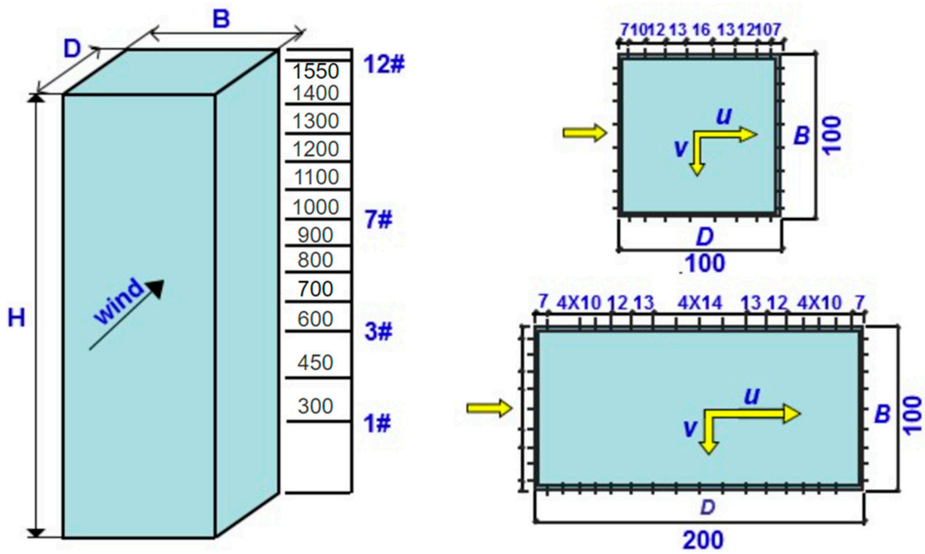


**Figure 2.** Layout of pressure taps. (unit: mm).

DSM3400 scanners with an acquisition accuracy of ±0.1% were installed inside each model, and they were used to simultaneously monitor surface pressures [6,11,14,19,31]. Data length can be used to satisfy the needs of spectral characterization, with a data sampling time of 120 s, and an acquisition frequency of 256 Hz. Direct pressure integration, for each pressure tap and their integral lengths, was used to determine the aerodynamic force of each layer.

The boundary layer turbulence flows were simulated using the traditional passive method, which involves arranging upstream spires and the surface roughness on the wind tunnel floor. For comparison, all tests were performed on two types of atmospheric boundary layer, named *BL*1 and *BL*2 flows, which represent the ground categories of open country and urban terrain (GB 50009-2012, Architectural Industry Press of China [32]), respectively. The measured mean wind velocity ($U_z$) and turbulence intensities ($I_u$) are shown in Figure 3, where $z_0$ is the reference height of the wind profile, $z_0 = 1.9$ m; $U_0$ is the reference mean velocity; and $z_z$ is the test height. The reference height of the pressure test was set at 3/4H of the model, that is, $z$ = 1.2 m, and the corresponding wind speed was approximately 9.6 m/s. The Reynolds number obtained from the test wind velocity and the rectangular model feature size was approximately $1.15 \times 10^5$, and its effect was ignored. The dimensionless power spectra of the turbulent fluctuation components in the along-wind and across-wind directions are shown in Figure 4. It is evident that the simulated boundary layer's turbulent flows can be fitted well using von-Karman's spectrum, and the integral length scale may be calculated by fitting this spectral model in the range of 1.1~1.42, which is basically consistent with the natural shear flows. The characteristic parameters of two turbulence fields are shown in Table 1.

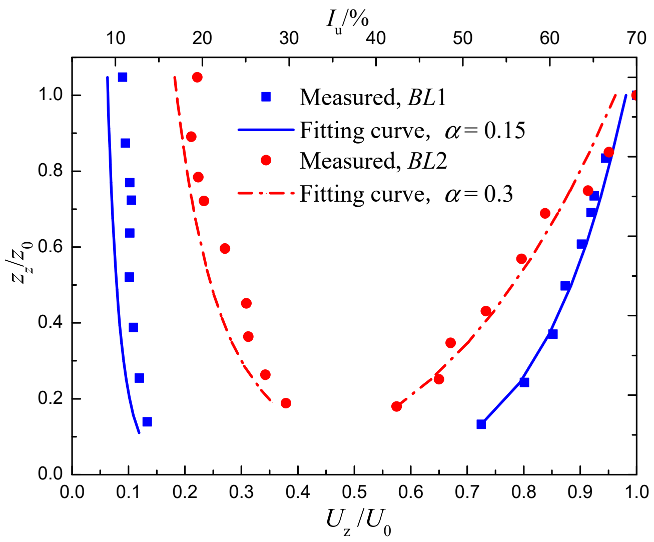


**Figure 3.** Mean wind and turbulence intensity profile.

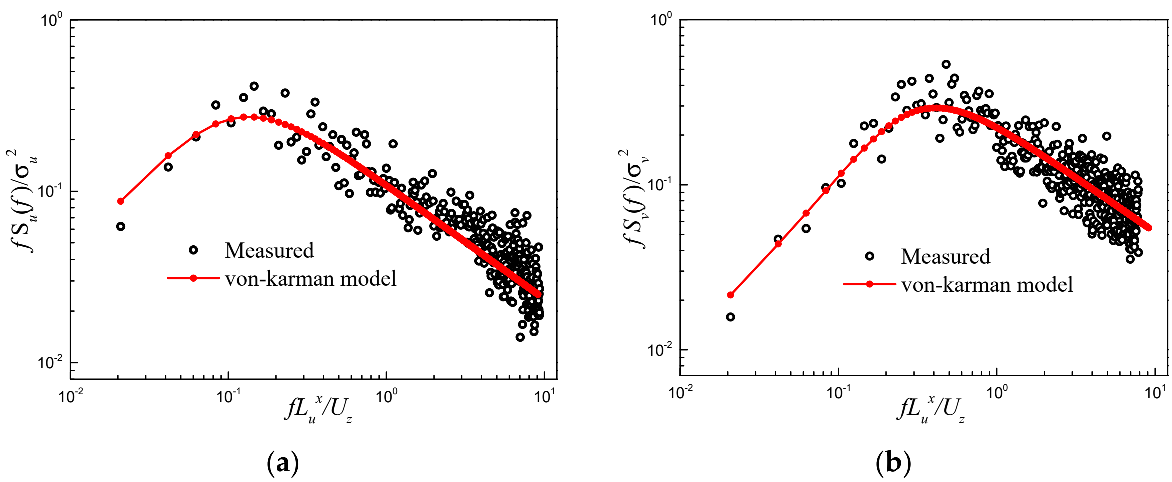


**Figure 4.** Normalized wind spectra at $z = 1.2$ m: (**a**) along-wind velocity component; (**b**) across-wind velocity component.

**Table 1.** Statistical parameters of the turbulence field ($z$ = 1.2 m).

| Wind Field Type | Integral Length Scale | | | Turbulence Intensity | | |
|---|---|---|---|---|---|---|
| | $L_u$ (m) | $L_v$ (m) | $L_w$ (m) | $I_u$ (%) | $I_v$ (%) | $I_w$ (%) |
| BL1 | 1.216 | 0.376 | 0.301 | 12.8 | 10.7 | 8.4 |
| BL2 | 1.027 | 0.324 | 0.232 | 27.1 | 22.1 | 18.3 |

## 3. Results and Discussion

### 3.1. Spectral Characteristics of Typical Pressure Taps

Following the measurement of the rectangular prisms' surface wind pressure time histories using the pressure measurement test, the Fast Fourier transform (FFT) method was used to determine the power spectral density. The spectral analysis of the wind pressure at typical pressure taps demonstrates the effects of the turbulence parameters, side ratio, geometric feature size, and three-dimensional flow on fluctuating aerodynamic forces; this aids in the investigation of energy production, transfer, and redistribution in various spatial locations [2,3,6,9,11,19,20,30]. The power spectrum characteristics of typical pressure taps with various side ratios are shown for rectangular prisms with a 9# layer at 3/4 height ($z$ = 1.2 m, Figure 2). Moreover, the dimensionless power spectrum of some pressure taps in the square prism is given in Figure 5, where $S_{pi}(f,z)$ is the power spectrum density function of the measurement points, $\sigma_{pi}$ is the root mean square (RMS) value of the pulsating wind pressure, and $U_z$ is the average velocity.

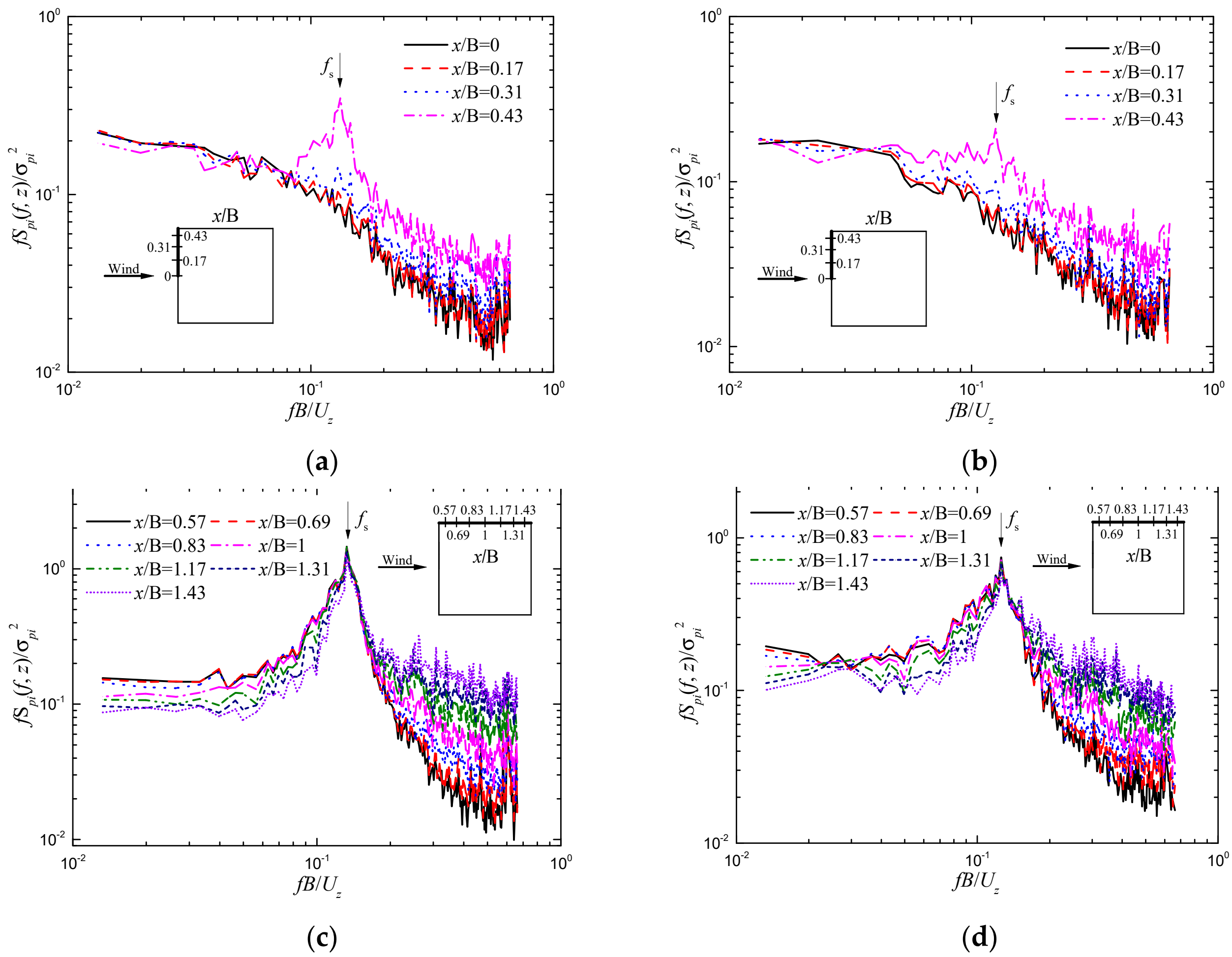


**Figure 5.** *Cont.*

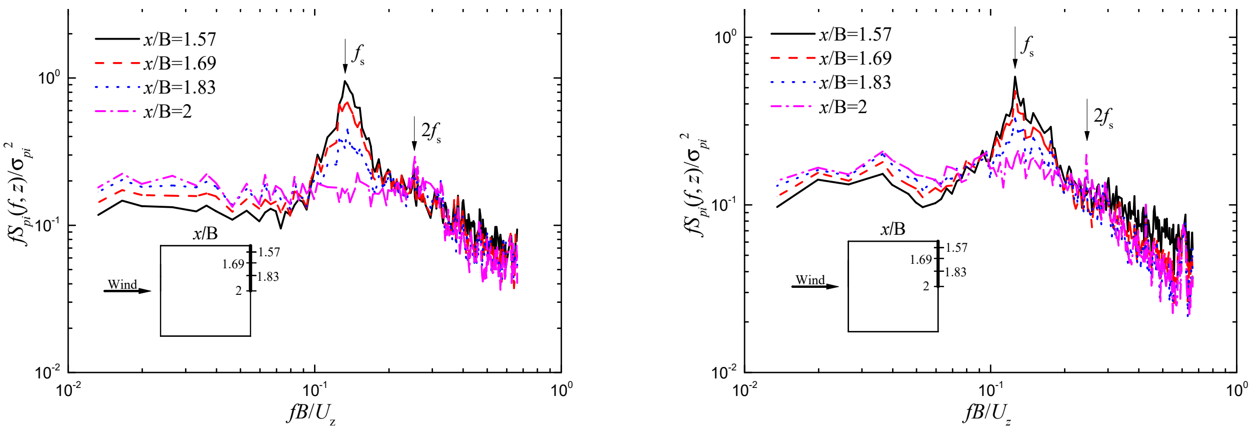


**(e)** **(f)**

**Figure 5.** The spectral density function of the typical pressure taps in the square prism: (**a**) windward side, *BL*1; (**b**) windward side, *BL*2; (**c**) lateral side, *BL*1; (**d**) lateral side, *BL*2; (**e**) leeward side, *BL*1; (**f**) leeward side, *BL*2.

The pressure taps in Figure 5 may be located using the dimensionless coefficient $x/B$, where $x$ is the separation distance between each tap and the stationary point. The power spectrum is primarily contorted via the incoming turbulence for the pressure taps on the windward side (Figure 5a,b), which is essentially proportional to the spectrum of the along-wind turbulence component [3,14,33]. The power spectrum exhibits a substantial peak as the distance from the windward corner decreases ($x/B = 0.43$), demonstrating that the action of vortex shedding steadily increases the variable nearby wind pressure.

The spectral characteristics of the fluctuating wind pressure on lateral sides are shown in Figure 5c,d. The spectral distribution trend is basically the same, with an obvious spectral peak near $f_s = 9.25$ Hz, and a Strouhal number of approximately $S_t = f_s B/U_z \approx 0.132$, indicating the presence of an obvious vortex shedding characteristic. At higher levels of turbulence intensity (*BL*2), the peak of the spectrum decreases to approximately half of what it was at the *BL*1 flow, but the spectral bandwidth increases significantly. This shows that as the turbulence intensity increases, the energy at the peak frequency is redistributed over a wider spectral bandwidth. Moreover, we discovered that the power spectrum varies depending on where it is located on the lateral side. As one moves away from the separation point, the low-frequency value of the spectrum sharply declines while the high-frequency value steadily rises. This phenomenon can be explained by the presence of large-scale, low-frequency vortices in the separated flow near the separation point; however, during the process of flowing downstream ($x/B = 0.57 \to 1.43$) the large-scale vortices are strongly disturbed by turbulence, broken up, and split into many smaller scale vortices of higher frequencies. These are accompanied by energy dissipation and transfer [3,6,13,19,20,25,34]. This process is more prominent in flows with higher turbulence intensities (*BL*2); in other words, they are flows with more extreme disruptions.

The variable wind pressure spectrum for the leeward pressure taps (Figure 5e,f) has a spectral peak at vortex shedding frequency $f_s$, suggesting that vortex shedding regulates the leeward aerodynamic force [3,6–8,13,19,20,25,35]. It should be noted, however, that the spectral peak lowers as the distance is reduced at the leeward side's midpoint, and the low-frequency value of the peak steadily rises. This suggests that when moving to the middle of the leeward side, the wake vortex is continuously absorbing the low-frequency fluctuation component energy, and the influence of the vortex shedding is gradually waning. Additionally, the asymmetry of vortex shedding may be the reason why the spectrum function towards the leeward side's midpoint has a smaller peak at $2f_s$, and why the turbulence intensities remain close to 30% (Figure 5f).

As is evident from Figure 6, a similar technique was used to study the wind pressure spectrum features of rectangular prisms with side ratios of $D/B = 1/2$ and 2. The spectrum properties of the fluctuating wind pressure are compatible with a square prism when the wide side is upwind ($D/B = 1/2$), as illustrated in Figure 6a,c,e. This suggests that under these operating conditions, the rectangular section's fluctuating wind pressure production and energy transfer mechanisms are similar to those of the square prism [3,8,14,28].

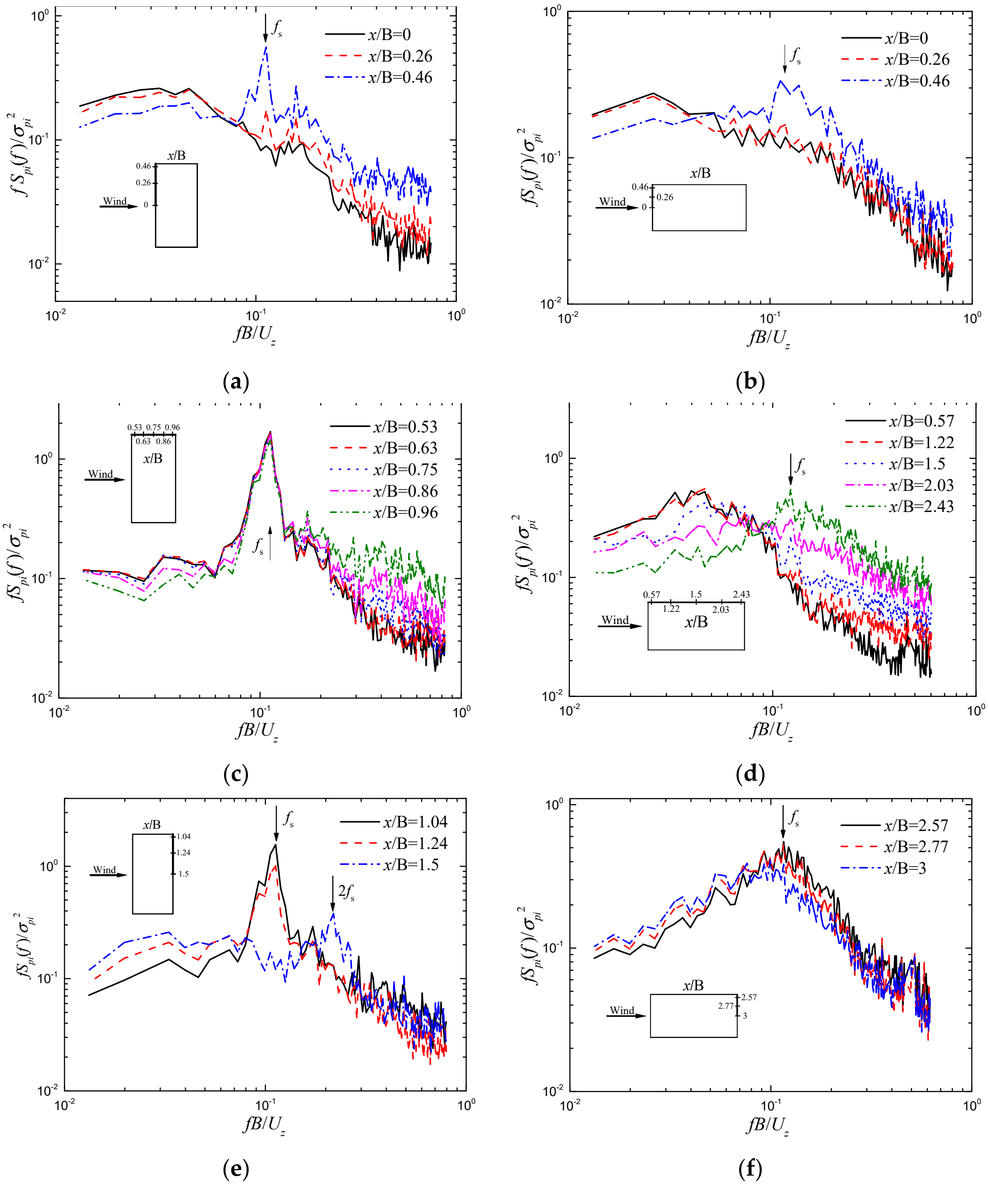


**Figure 6.** Spectra of typical pressure taps with $D/B = 2$ and $1/2$: (**a**) windward side, $D/B = 1/2$; (**b**) windward side, $D/B = 2$; (**c**) lateral side, $D/B = 1/2$; (**d**) lateral side, $D/B = 2$; (**e**) leeward side, $D/B = 1/2$; (**f**) leeward side, $D/B = 2$.

As shown in Figure 6b,d,f, when the narrow side is facing the wind ($D/B = 2$), it is possible for the separated shear flow to reattach under conditions of high-level turbulence intensity, which would significantly alter the spectrum features. The turbulent flow disturbance increases the separation shear flow's coiling influence on the free mean fluid in the return zone as the pressure tap moves away from the separation point. The fluctuating wind pressure energy is transported from the peak frequency to a larger spectral bandwidth as a result of the interference between the turbulent components, separated and reattached flows, various scale vortices, and the frequent energy exchange. The reattachment flow may divide once more when the pressure taps near the tail of the lateral side exhibit the spectral peak of the vortex shedding feature; despite this, the high-frequency value of the fluctuating pressure spectrum in this area still increases. Overall, the interference of the separated shear flow reattachment, and the entering turbulence, changes the fluctuating pressure spectrum features, similarly to those under vortex shedding control.

Studies in this field have shown that the separated shear flow will reattach on the lateral side, whereas the comparable side ratio in the uniform flow is approximately $D/B$ = 2.8 [19,30,35,36]. However, the incoming turbulent flow disturbances increase the curvature of the separation shear layer, further compressing the size of the primary vortex in the separation zone; this causes the reattachment phenomena to manifest earlier, at smaller side ratios, such as $D/B$ = 2 in the current study. The larger-scale vortices in the shear flow are quickly broken into smaller-scale vortices as a result of the lateral sides' stretching, squeezing, and dragging effects on the vortices. This results in spectral characteristics that differ from those controlled by vortex shedding. The intrinsic relationship between flow phenomena like turbulence, separation, and reattachment flow, and vortex shedding and aerodynamic forces, could not be visually investigated in this study due to the limitations of the experimental conditions; instead, this was primarily hypothesized and summarized through pressure measurement tests.

The flow around the regime and properties of the aerodynamic spectrum becomes more complex as the magnitude of the lateral spreading continues to grow. In Figure 7, the aerodynamic mechanism and energy transfer of the rectangular section with large side ratios are first examined using the rectangular prism with $D/B$ = 3 and 1/3 in the $BL1$ flow as an example. The spectral characteristics of the fluctuating wind pressure at the windward pressure taps are basically the same as those of the other rectangular prisms (Figure 7a), with the same fluid separation and vortex shedding at the windward corner, which is accompanied by a reduction in the low-frequency value, and an increase in the high-frequency value of the power spectrum.

Given the lateral side's extensive spreading length, it is split into two pieces, starting from a location close to the potential point of reattachment ($x/B = 1.54$) (see Figure 7b,c). This portion is in the inner zone, before the separation flow is reattached (Figure 7b). Moreover, separation bubbles present in this area are attached to the lateral side at the inner zone's midpoint, which is also the location of the lateral side's highest negative wind pressure ($x/B = 0.82$). Although the high-frequency value steadily rises, and the spectrum peak at the vortex shedding frequency gradually reaches its maximum, the low-frequency value of the power spectrum declines and reaches a minimum near the midpoint of the inner area. It should be noted that the inner zone's fluctuating pressure spectrum properties differ dramatically from those of the apparent vortex shedding. These phenomena are particularly prominent in high-level turbulence intensity flows ($BL2$), where incoming turbulence causes the large-scale vortices in the separated flow to be squeezed and stretched, prompting the energy to be redistributed to a wider spectral bandwidth. The spectral peak value drops by approximately 75% when the side ratio is raised from 1 to 3, although less than 15% of the energy of the fluctuating wind pressure is lost overall. The low-frequency values of the spectrum begin to pick up again between the point that is halfway downstream of the inner zone and the reattachment point, whereas the high-frequency values remained mostly unchanged. In terms of energy change, the variable wind pressure spectrum in this area has a rising energy that peaks nearby to the reattachment point ($x/B = 1.54$). This finding shows that the high-frequency, small-scale vortices dissipate and are less affected by it; rather, they are primarily controlled by the larger-scale, low-frequency vortices, due to the increase in the curvature of the separated shear layer and the continuous absorption of energy from turbulent fluctuations [3,6,7,9,11,18–20].

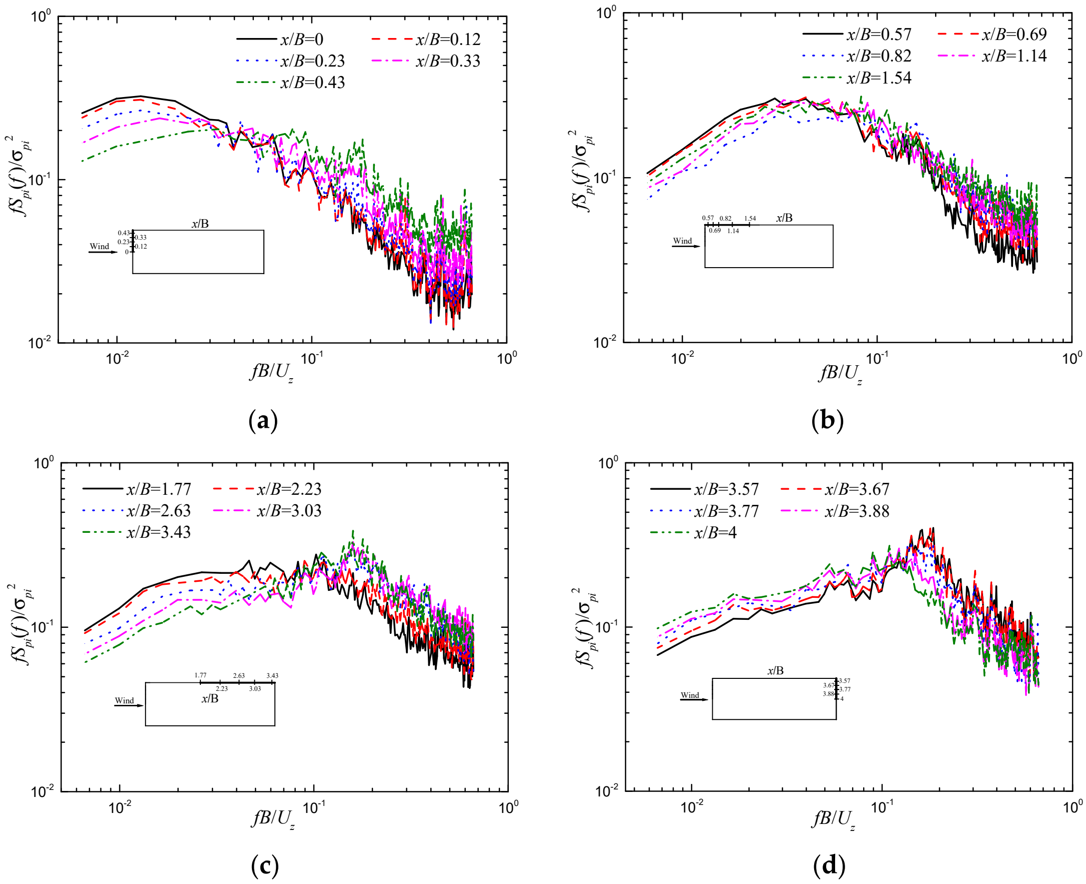


**Figure 7.** Spectra of typical pressure taps with $D/B = 3$: (**a**) windward side; (**b**) front part of the lateral side; (**c**) rear part of the lateral side; (**d**) leeward side.

The low-frequency values of the spectrum degrade quickly in the region downstream of the reattachment point (Figure 7c), whereas the high-frequency variations gradually rise. These phenomena are clear examples of separation shear flow reattachment, wherein energy is transferred from low-frequency to high-frequency wind pressure fluctuations. The spectral peak of the fluctuating wind pressure sharply rises as it approaches the corner point of the tail ($x/B = 3.16 \rightarrow 3.43$), suggesting that the reattachment fluid may become separated once more. According to Figure 7d, the results for the pressure taps on the leeward side are mostly influenced by the development of distinctive turbulence, caused by secondary separation; this is comparable to the spectrum features for $D/B = 2$.

By summarizing the characteristics of fluctuating wind pressure spectra, the flow-solid interaction and aerodynamic mechanism of rectangular prisms with varying side ratios, under boundary layer turbulence, are explored. The three-dimensional flow condition surrounding the bluff body, particularly the vortex shedding and separated reattachment flow occurring on the lateral side, is already complex, and an accurate explanation of the condition is made more challenging due to the perturbation caused by the boundary layer turbulence [2,3,6,8,9,13,19,23,33]. Although the mechanism and energy changes of aerodynamic forces can be visually reflected by the power spectrum analysis of fluctuating wind pressure, many subtleties of flow phenomena cannot be reflected, and a more in-depth quantitative investigation may be conducted in the future using PIV or CFD methods [23,25,28,29,36].

### 3.2. Spectral Characteristics of Fluctuating Aerodynamic Forces

The fluctuating aerodynamic forces in three directions (along-wind fluctuating load, across-wind fluctuating load, and torque) are obtained using a direct integration method. Fluctuating wind pressure and the corresponding integration length provide the straightforward aerodynamic shape of the rectangular prism. The pressure tap layers at the model's bottom (1#), 2/3H (8#), and upper half (11#) were selected to provide the power spectrum functions of the fluctuation aerodynamics of rectangular prisms under various boundary layer turbulence conditions. The along-wind fluctuation load, the across-wind load, and the torque dimensionless power spectra for the rectangular prism with $D/B$ = 1/3, are shown in Figures 8 and 9. In these figures, $S_D(f,z)$, $S_L(f,z)$, and $S_T(f,z)$ represent the three component fluctuation aerodynamic spectra; $\sigma_D$, $\sigma_L$, and $\sigma_T$ are the root mean square; $V_H$ is the average velocity at the top of the model.

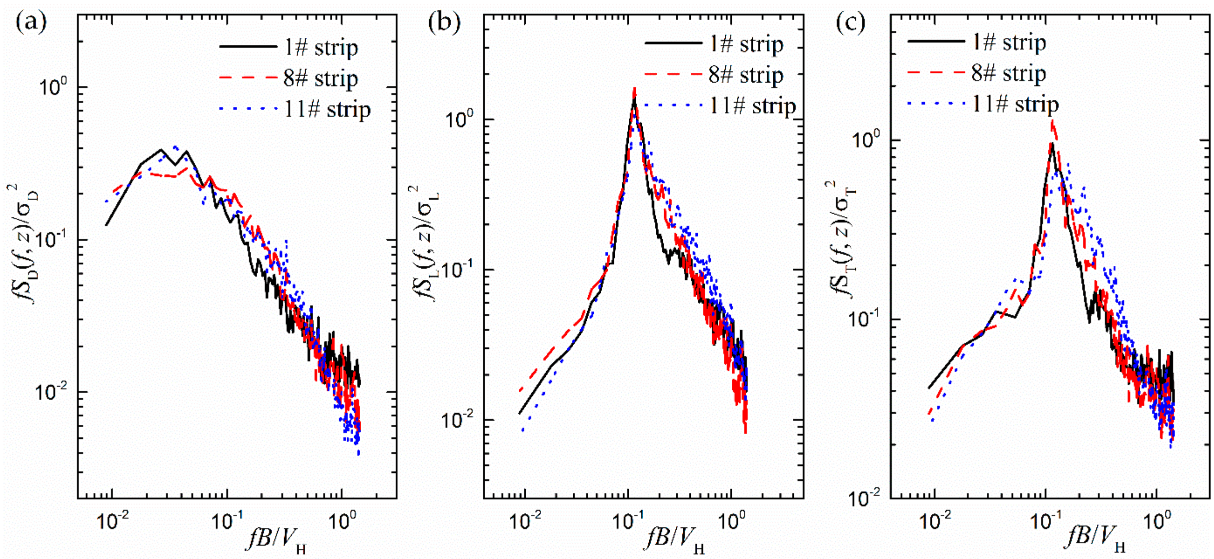


**Figure 8.** The dimensionless power spectra of fluctuating aerodynamic forces with $D/B$ = 1/3 in $BL1$: (**a**) along-wind fluctuating load; (**b**) across-wind fluctuating load; (**c**) torque.

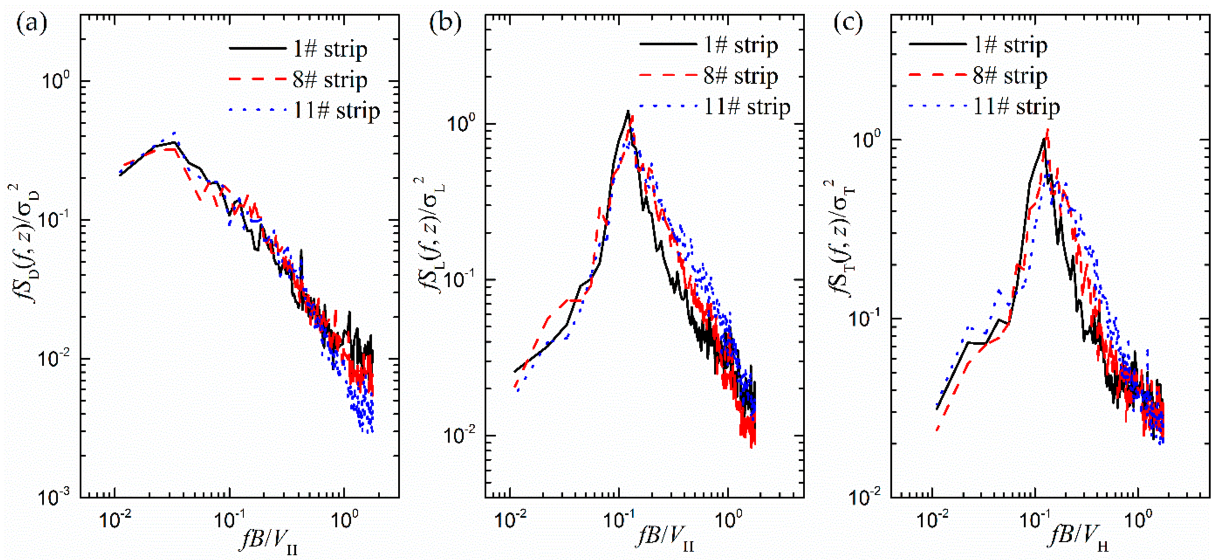


**Figure 9.** The dimensionless power spectra of fluctuating aerodynamic forces with $D/B$ = 1/3 in $BL2$: (**a**) along-wind fluctuating load; (**b**) across-wind fluctuating load; (**c**) torque.

There is substantial consistency in terms of the fluctuating aerodynamic spectrum of rectangular prisms when the width of the windward side is greater than the downstream spreading length ($D/B$ < 1). According to Figures 8a and 9a, the along-wind turbulent component primarily affects the along-wind fluctuating wind load, which is more severely affected in the low frequency range. The across-wind fluctuating wind load and torque are largely defined by vortex shedding, and the spectrum contains spectral peaks that are comparable to the characteristics of the fluctuating wind pressure spectrum [2–4,9,13,14,19,25,28,33]. The power spectrum is primarily affected by the weakening of the low frequency area. The high-frequency fluctuations are augmented as the wind field turbulence intensity increases, and the energy is distributed over a larger spectral bandwidth. The experimental results further demonstrate the impact of end effects on fluctuating wind loads, with reduced power spectrum values, at roughly 0.12 Hz. The fact that these phenomena are more noticeable in the $BL1$ suggests that the alteration of turbulence characteristics interferes with vortex shedding and top flow in a significant manner.

The fluctuating aerodynamic spectra of the square prism are closer to those of the rectangular prism as they have a small side ratio ($D/B < 1$), as shown in Figure 10. It should be observed, nonetheless, that the torque also has a smaller spectral peak at $2f_s$, and it is more substantial near the top of the model in $BL2$. In addition, it also has a significant spectral peak at the vortex shedding frequency, as shown in Figure 10c. This may be occur due to the occasional reattachment of the separated flow that is already present and facilitated by the end effect; however, this study did not adequately document these flow specifics.

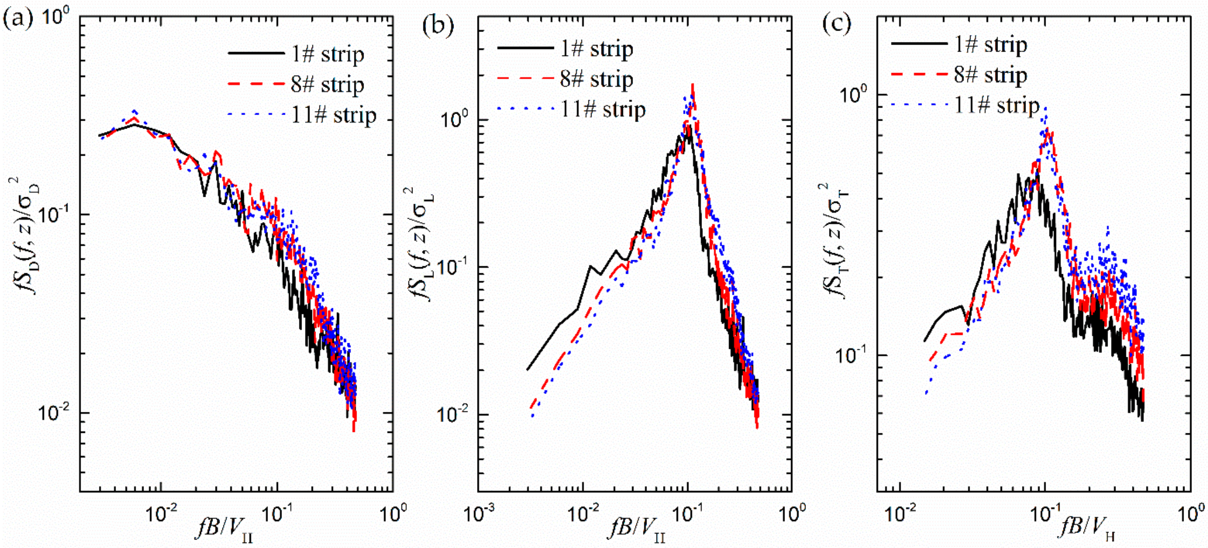


**Figure 10.** The dimensionless power spectra of fluctuating aerodynamic forces on the square prism in $BL2$: (**a**) along-wind fluctuating load; (**b**) across-wind fluctuating load; (**c**) torque.

The power spectra at $D/B = 4$ are shown in Figures 11 and 12, and as the side ratio of the rectangular prism grows (that is, as the downstream spread exceeds the windward width), its fluctuating aerodynamic spectra exhibit distinct characteristics.

The results given in the preceding section indicate that for rectangular prisms with large side ratios ($D/B \geq 2$), there are notable changes in the fluctuating wind pressure spectra, primarily on the lateral and leeward sides. The spectral properties of the torque and across-wind fluctuating wind load are mainly impacted by the aforementioned variances. When the side ratio $D/B$ hits 2, the separated shear flow reattaches to the lateral sides under the effects of turbulent flow, resulting in a reduced spectral peak and an increase in the spectral bandwidth. However, with various turbulent entering flows, there are differences in variation tendencies. Although the fixed value of $BL2$ is reached earlier, at $D/B = 2$, for $BL1$, the bandwidth of the across-wind fluctuating wind load and torque spectrum is essentially fixed until $D/B$ reaches 3. This finding suggests that one of the key elements contributing to the separated shear flow's early reattachment is the increased turbulence intensity of the wind field [6–9,16,18–21,24,25]. Additionally, when the separated flow reattachment takes place on the lateral side, the across-wind fluctuating wind load spectra display a lower spectral peak that is close to the approximate frequency of 0.2. This spectral peak could be the result of a subsequent shedding of the reattached separating shear layer at the back of the lateral side, which would produce the signature wake turbulence. When the turbulence intensity rises, the across-wind fluctuating wind load spectrum's bandwidth expands noticeably, and the value of the second peak falls. This demonstrates that the disturbance effect of the higher turbulence intensity is enhanced, and different kinds of small-scale vortices continuously dissipate as they move downstream. The across-wind fluctuating wind load spectra in the vertical direction are more similar at low frequencies, but the second spectral peak (towards the top) is higher because of the presence of a non-negligible end effect.

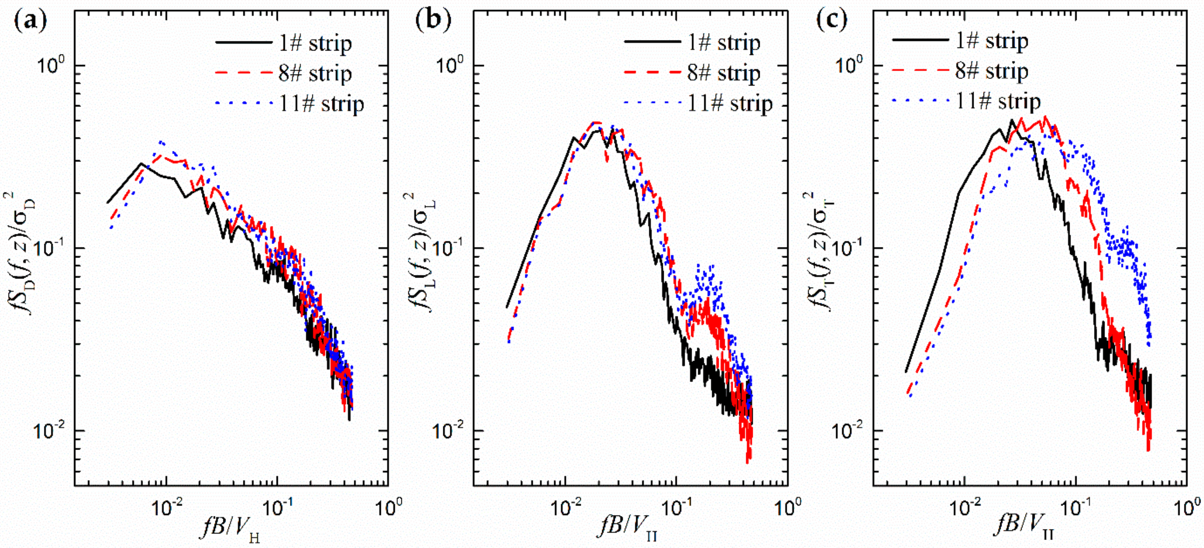


**Figure 11.** The dimensionless power spectra of fluctuating aerodynamic forces with $D/B$ = 4 in $BL1$: (**a**) along-wind fluctuating load; (**b**) across-wind fluctuating load; (**c**) torque.

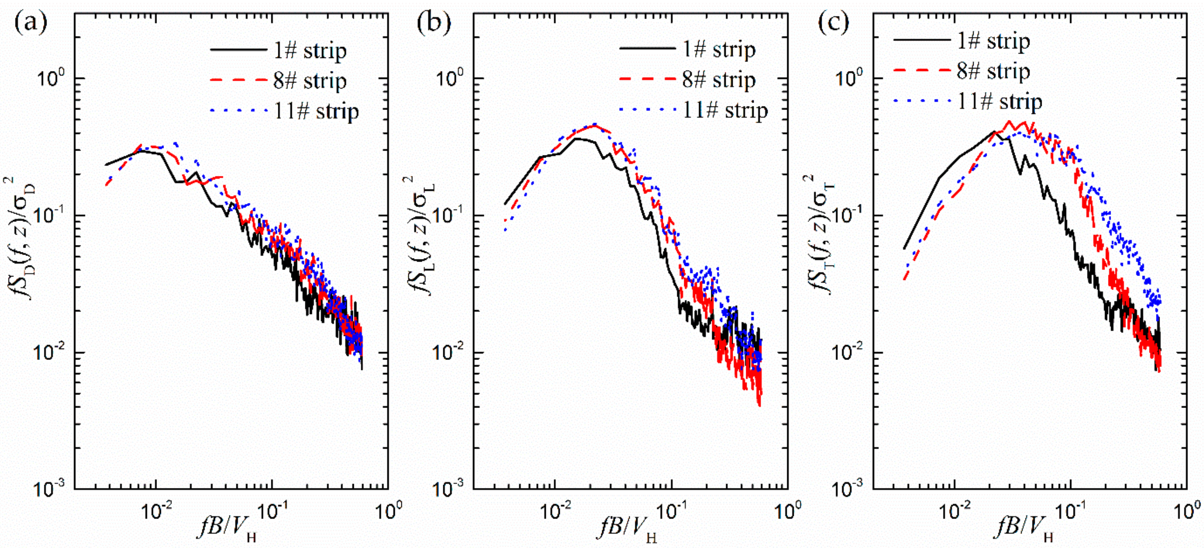


**Figure 12.** The dimensionless spectral functions of fluctuating aerodynamic forces with $D/B$ = 4 in $BL2$: (**a**) along-wind fluctuating load; (**b**) across-wind fluctuating load; (**c**) torque.

In general, the power spectrum parameters for the torque of rectangular prisms are more akin to those of across-wind fluctuating wind loads. Torque-related studies are still comparatively scarce and still not fully understood because of the complicated aerodynamic mechanism underlying torque.

In this section, the fluctuating aerodynamic forces and spectrum characteristics of rectangular prisms are analyzed based on experimental results, and the role of influencing factors such as turbulence parameters, side ratios, end effects, and various flow phenomena are discussed. Overall, the along-wind fluctuating wind load of the rectangular prism is mainly controlled by incoming turbulence, and its power spectrum is proportional to the along-wind fluctuating velocity spectrum. The aerodynamic mechanisms of the across-wind fluctuating load and torque are more complex, and the turbulent boundary layer flow, side ratio, vortex shedding, separation and reattachment flow, and end effects all have important effects on these mechanisms. However, it is not yet possible to fully understand how large-scale turbulence interferes with the separation flow, the change in the size of the separation bubble, the location of the reattachment point and secondary separation point, and how the vortices move on different scales, among other phenomena. At the same time, due to the limitations of the experimental methodology employed, this study has not yet been able to fully reveal the specific roles of the influencing factors, and the cross-correlations between the factors and their combined effects could not be explored in depth. The across-wind aerodynamic spectral properties and their influencing factors can be further investigated by utilizing more effective research tools, such as CFD or PIV methods.

### 3.3. Normalized Across-Wind Fluctuating Load Spectrum Model

As one of the primary tasks of wind-induced structural response computation, selecting an appropriate and accurate spectrum model for fluctuating wind load is needed to accurately assess various wind effects. Based on the quasi-definite theory and strip assumption, the generalized aerodynamic spectrum for the fluctuating along-wind load is generated by converting the along-wind turbulence component. However, the spectral properties of the fluctuating across-wind load and torque are more complex, and the quasi-definite theory is thus no longer applicable. Therefore, various empirical models are created by fitting the experimentally observed spectrum.

Previous analyses have found that although a number of factors can affect the fluctuating across-wind load spectrum, its relationship with the side ratio of the rectangular prism from the flow around state is particularly strong. The fluctuating wind load spectrum is a narrow-band phenomenon with a spectral peak, and it is primarily governed by vortex shedding at small side ratios ($D/B < 2$). When the side ratio is sufficiently large ($D/B \geq 2$), the separated shear flow reattachment causes the aerodynamic force spectral energy to be redistributed to a wider bandwidth, leading to a broadband process with a petite spectral peak in the fluctuating wind load spectrum. Based on this feature concerning the fluctuating across-wind load spectral function, and with reference to existing spectral models [3,6–9,16,18–22,24,25,37,38], this study provides an empirical formula based on the side ratio of rectangular prisms. These expressions are as follows:

$$\frac{fS_L(f)}{\sigma_L^2} = \sum_{i=1}^{N} \frac{\beta_i \cdot (f/f_{si})^2}{\left[1-((f/f_{si})^2)\right]^2 + 4\beta_i^2 \cdot (f/f_{si})^2} + \eta \cdot \exp\left\{-[\alpha_1 - \alpha_2 \cdot (f/f_{si})^2]\right\} \tag{1}$$

where, $N$ is the parameter related to the side ratio when $D/B < 2$, $N = 1$ and when $D/B \geq 2$, $N = 2$; $\beta_i$ is the spectral bandwidth correction factor; $\eta$ is the spectral peak adjustment factor; $f_{si}$ is the vortex shedding frequency; $\alpha_1$ and $\alpha_2$ are the low-band and high-band fluctuation correction parameters, respectively. The nonlinear least squares method was used to fit the experimental data to obtain the determined parameters, as follows:

$$\beta_1 = -0.13 \cdot \left({}^{D}\!/_{B}\right)^3 + 0.927 \cdot \left({}^{D}\!/_{B}\right)^2 - 1.707 \cdot {}^{D}\!/_{B} + 1.051 \tag{2}$$

$$\beta_2 = 0.383 \cdot {}^{D}\!/_{B} - 0.05 \tag{3}$$

$$f_{s1} = 1.488 \cdot \left({}^{D}\!/_{B}\right)^3 - 10.581 \cdot \left({}^{D}\!/_{B}\right)^2 + 18.996 \cdot {}^{D}\!/_{B} - 0.257 \tag{4}$$

$$f_{s2} = -1.395 \cdot {}^{D}\!/_{B} + 9.142 \tag{5}$$

$$\eta = -0.063 \cdot \left({}^{D}\!/_{B}\right)^3 + 0.555 \cdot \left({}^{D}\!/_{B}\right)^2 - 1.52 \cdot {}^{D}\!/_{B} + 1.146 \tag{6}$$

$$\alpha_1 = -0.685 \cdot \left({}^{D}\!/_{B}\right)^3 + 5.706 \cdot \left({}^{D}\!/_{B}\right)^2 + 13.808 \cdot {}^{D}\!/_{B} + 9.812 \tag{7}$$

$$\alpha_2 = -1.051 \cdot \left({}^{D}\!/_{B}\right)^3 + 8.61 \cdot \left({}^{D}\!/_{B}\right)^2 - 21.222 \cdot {}^{D}\!/_{B} + 14.783 \tag{8}$$

According to the aforementioned empirical model, the results of the measured spectral functions are displayed in Figure 13. They demonstrate that the fit is good and can generally explain the spectrum characteristics of various side ratios. It is evident that the fitting accuracy is high because the proposed empirical formula considers the effects of the flow-induced high-frequency fluctuations and spectral bandwidth changes caused by the incoming turbulence, side ratio, vortex shedding, and separation reattachment. As illustrated in Figure 14 (the formulas used are presented in Appendix A), a comparison between the proposed formula and the existing common empirical models is made to further demonstrate the applicability of the formula.

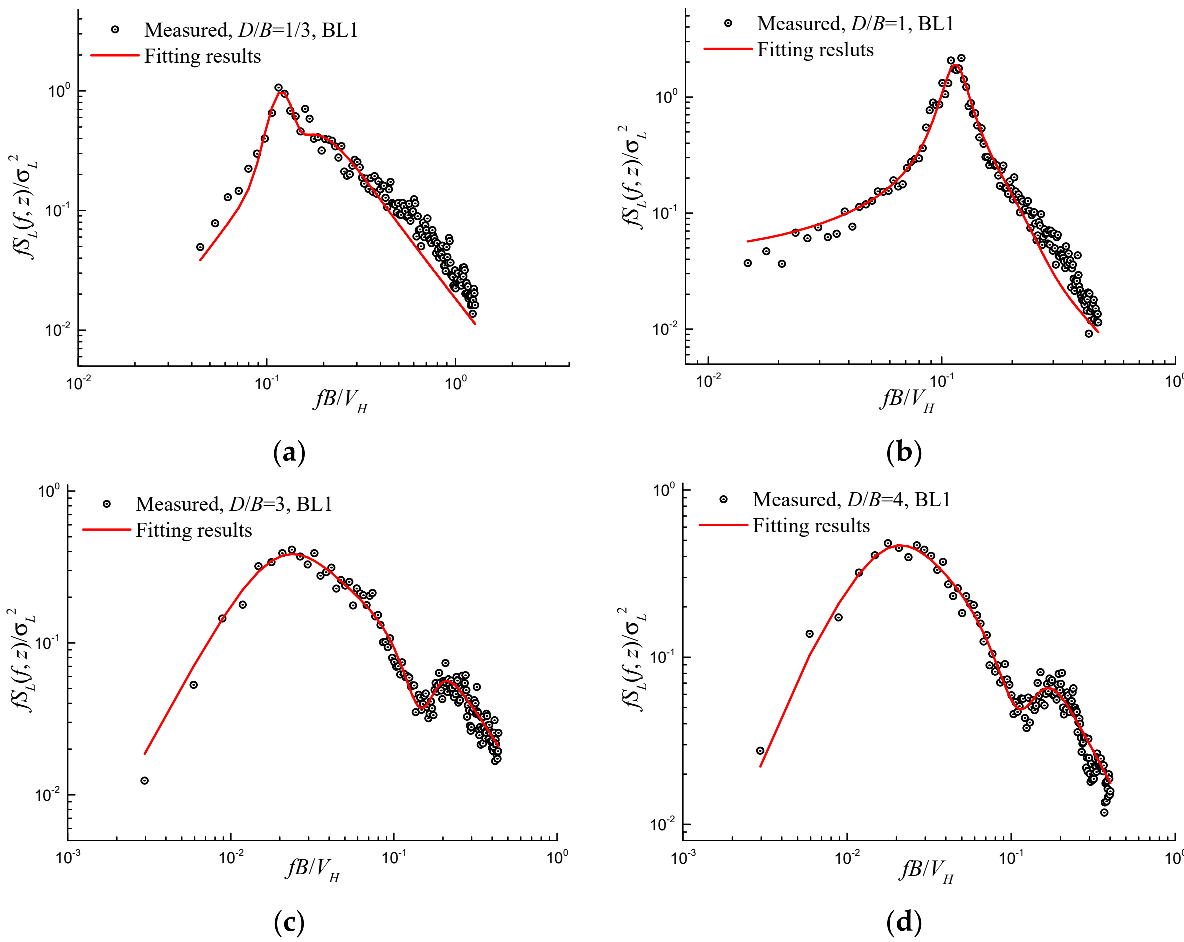


**Figure 13.** Fitting of dimensionless spectra of rectangular prisms with different side ratios: (**a**) $D/B = 1/3$; (**b**) $D/B = 1$; (**c**) $D/B = 3$; (**d**) $D/B = 4$.

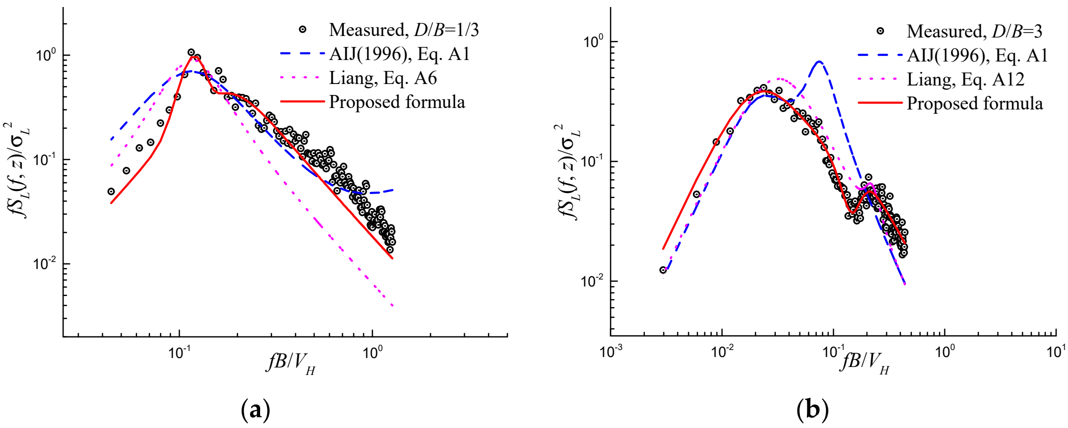


**Figure 14.** Comparison of the proposed formula with the classical spectral models: (**a**) $D/B = 1/3$; (**b**) $D/B = 3$.

By comparing the theoretical formulations offered by AIJ [24] (Equation (A1)) and Liang [6] (Equations (A6) and (A12)), it is further shown that their models are valid and that they adequately explain the fundamental properties of the spectrum. However, there are still limitations in terms of defining the specifics of the recorded fluctuating aerodynamic force spectrum; this is because of the associated application range and criteria for the aforementioned models. One of the most popular models is the empirical formula provided by AIJ, which has excellent expression accuracy when small side ratios ($D/B < 3$) are used, but it produces high estimations of spectral peaks and high band values when bigger side ratios ($D/B \geq 3$) are used. Although Liang's empirical formula for characterizing spectral features is based on variations in the side ratio, there are still some discrepancies in terms of how it describes the high-frequency band and the second spectral peak. After summarizing these methods, it is clear that the existing models lack a sufficient understanding of the impact of large-scale boundary layer turbulence on the complex flow surrounding rectangular prisms and their spectral characteristics; this makes it impossible to describe the spectral peaks, spectral bandwidth, and energy variations. The fluctuating aerodynamic force spectra of rectangular prisms, with different side ratios, were the subject of this experimental study, which contributed to a deeper understanding of the flow phenomena and aerodynamic mechanisms surrounding these prisms. A wide range of applications are possible for the proposed empirical formula, which may be enhanced and validated in subsequent studies. Furthermore, it should be noted that the empirical model proposed in this study was only obtained based on the pressure tests of seven rigid models, and thus, its applicability needs to be further verified.

## 4. Conclusions

In this study, seven prismatic building models, with different side ratios, were tested in a wind tunnel. The spectra of the aerodynamic force fluctuations were obtained and compared with existing empirical models. Regarding the aerodynamic load spectrum features, the effects of the turbulence intensity, vortex shedding, side ratio, and separation and reattachment flows were explored. The following conclusions can be drawn:

(1) The reattachment characteristic may already be observed for $D/B = 2$ when the turbulence fluctuation level is significant, indicating that a turbulent disturbance will cause the reattachment phenomena to occur earlier, at a smaller side ratio.
(2) The separated shear flow reattachment causes the aerodynamic force spectral energy to be redistributed over a wider bandwidth, which results in a broadband process with a reduced spectral peak when the side ratio is reasonably large ($D/B \geq 2$).
(3) It is suggested that a more realistic normalized spectral model for the across-wind fluctuating load is used; this model should take into account incoming turbulence,

side ratios, spectral bandwidth changes (caused by vortex shedding and separated reattachment flows), and high-frequency fluctuations, among other factors.

**Author Contributions:** Conceptualization, methodology, software, and writing, J.Z.; Investigation and validation, J.Z. and S.L.; Resources, supervision, and revision, M.L. and Z.Z. All authors have read and agreed to the published version of the manuscript.

**Funding:** This research was funded by the Hainan Provincial department of Science and Technology Fund Project, grant Numbers 520RC545, 520CXTD433 and 623RC451, the National Natural Science Foundation of China, grant Number 52068020, 51938012 and 52268073.

**Institutional Review Board Statement:** Not applicable.

**Informed Consent Statement:** Not applicable.

**Data Availability Statement:** Not applicable.

**Acknowledgments:** The authors gratefully acknowledge the support of the Hainan Provincial department of Science and Technology Fund Project (Grant Nos. 520RC545, 520CXTD433 and 623RC451), and the Authors are also indebted to the National Natural Science Foundation of China for research projects granted in recent years (Grant Nos. 52068020, 51938012 and 52268073). We thank the reviewers and the editor for the valuable comments and suggestions that helped us improve the manuscript.

**Conflicts of Interest:** The authors declare no conflict of interest.

## Appendix A

The more widely used across-wind aerodynamic spectrum model for rectangular high-rise buildings is the empirical formula based on Japanese design recommendations [24], which is expressed as follows:

$$\frac{fS_L(f)}{\sigma_L^2} = \sum_{i=1}^{N} \left\{ \frac{2k_i\beta_i \cdot (1+0.6\beta_i)}{\pi} \times \frac{(f/f_{si})^2}{\left[1-(f/f_{si})^2\right]^2 + 4\beta_i^2 \cdot (f/f_{si})^2} \right\}, \tag{A1}$$

where $N = 1$ when $D/B < 3$, and $N = 2$ when $D/B \geq 3$; $k_1 = 0.85$, $k_2 = 0.02$.

The vortex shedding frequency $f_{si}$ is related to the side ratio, and its expression is as follows:

$$f_{s1} = \frac{0.12}{\left[1+0.38 \cdot (D/B)^2\right]^{0.89}}, \tag{A2}$$

$$f_{s2} = \frac{0.56}{(D/B)^{0.85}}, \tag{A3}$$

where $\beta_i$ is the coefficient related to the spectral bandwidth, which can be calculated using the following equation:

$$\beta_1 = \frac{(D/B)^4}{1.2(D/B)^4 - 1.7(D/B)^2 + 21} + \frac{0.12}{D/B}, \tag{A4}$$

$$\beta_2 = 0.28 \cdot (D/B)^{-0.34}. \tag{A5}$$

An improved spectrum model was provided by Liang [6], which fitted the experimental data, and it was represented in terms of side ratio segmentation. When $1/4 \leq D/B < 3$, the equation is as follows:

$$\frac{fS_L(f)}{\sigma_L^2} = A \cdot \frac{H(C_1)\overline{f}^2}{(1-\overline{f}^2) + C_1\overline{f}^2} + (1-A)\frac{C_2^{1/2}\overline{f}^3}{1.56 \cdot \left[(1-\overline{f}^2)^2 + C_2\overline{f}^2\right]}, \tag{A6}$$

where the parameters can be calculated using the following equations:

$$H(C_1) = 0.179C_1 + 0.65\sqrt{C_1}, \tag{A7}$$

$$C_1 = [0.47(D/B)^{2.8} - 0.52(D/B)^{1.4} + 0.24]/(H/\sqrt{S}), \tag{A8}$$

$$C_2 = 2. \tag{A9}$$

and when $1/4 \leq D/B < 1/2$,

$$A = (H/\sqrt{S}) \cdot [-0.6(D/B)^2 + 0.29(D/B) - 0.06] + [9.84(D/B)^2 - 5.86(D/B) + 1.25], \tag{A10}$$

when $1/2 \leq D/B < 3$

$$A = (H/\sqrt{S}) \cdot [-0.118(D/B)^2 + 0.358(D/B) - 0.214] + [0.066(D/B)^2 - 0.26(D/B) + 0.894], \tag{A11}$$

in which, $\overline{f} = f/f_s$.

When $1/4 \leq D/B < 3$, the equation is as follows:

$$\frac{fS_L(f)}{\sigma_L^2} = A \cdot \frac{1.275 \cdot \overline{f}^2}{(1-\overline{f}^2) + C_1\overline{f}^2} + (1-A)\frac{C_2^{1/2}(\overline{f}/k)^3}{1.56 \cdot [(1-(\overline{f}/k)^2)^2 + C_2(\overline{f}/k)^2]}, \tag{A12}$$

where the parameters can be calculated using the following equations:

$$k = -0.175 \cdot (H/\sqrt{S}) + 4.7 \quad 4 \leq H/\sqrt{S} \leq 8, \tag{A13}$$

$$C_1 = 2, \tag{A14}$$

$$C_2 = 2/k, \tag{A15}$$

$$A = aI_u^b, \tag{A16}$$

$$a = 0.17 \cdot (H/\sqrt{S}) + 3.32, \tag{A17}$$

$$b = 0.18 \cdot (D/B) + 0.26. \tag{A18}$$

## References


1. Davenport, A.G.; Agnew, R.; Harris, R.I.; Sachs, P. The application of statistical concepts to the wind loading of structures. *ICE Proc.* **1961**, *19*, 449–472. [CrossRef]
2. Kareem, A. Measurements of pressure and force fields on building model in simulated atmospheric flows. *J. Wind Eng. Ind. Aerodyn.* **1990**, *36*, 589–599. [CrossRef]
3. Dyrbye, C.D.; Hansen, S.O. *Wind Loads on Structures*; John Wiley & Sons, Ltd.: Hoboken, NJ, USA, 1997; pp. 36–44.
4. Li, M.S.; Yang, Y.; Li, M.; Liao, H.L. Direct measurement of the Sears function in turbulent flow. *J. Fluid Mech.* **2018**, *847*, 768–785. [CrossRef]
5. Lou, W.J.; Zhang, L.G.; Huang, M.F.; Li, Q.S. Multiobjective Equivalent Static Wind Loads on Complex Tall Buildings Using Non-Gaussian Peak Factors. *J. Struct. Eng.* **2015**, *141*, 04015033. [CrossRef]
6. Liang, S.; Liu, S.; Li, Q.; Zhang, L.; Gu, M. Mathematical model of acrosswind dynamic loads on rectangular tall buildings. *J. Wind Eng. Ind. Aerodyn.* **2002**, *90*, 1757–1770. [CrossRef]
7. Kareem, A. Model for predicting the acrosswind response of buildings. *Eng. Struct.* **1984**, *6*, 136–141. [CrossRef]
8. Choi, H.; Kanda, J. Proposed formulae for the power spectral densities of fluctuating lift and torque on rectangular 3-D cylinders. *J. Wind Eng. Ind. Aerodyn.* **1993**, *46*, 507–516. [CrossRef]
9. Gu, M.; Quan, Y. Across-wind loads of typical tall buildings. *J. Wind Eng. Ind. Aerodyn.* **2004**, *92*, 1147–1165. [CrossRef]

10. Gu, M.; Quan, Y. Across-wind loads and effects of super-tall buildings and structures. *Sci. China Technol. Sci.* **2011**, *54*, 2531–2541. [CrossRef]
11. Li, S.P.; Li, M.S.; Liao, H.L. The lift on an aerofoil in grid-generated turbulence. *J. Fluid Mech.* **2015**, *771*, 16–35. [CrossRef]
12. Yang, Y.; Li, M.S.; Ma, C.M.; Li, S.P. Experimental investigation on the unsteady lift of an airfoil in a sinusoidal streamwise gust. *Phys. Fluids* **2017**, *29*, 051703. [CrossRef]
13. Duan, F.C.; Song, Y.; Gao, S.B.; Liu, Y.H.; Chu, W.P.; Lu, X.B.; Liu, Z.G. Study on Aerodynamic Instability and Galloping Response of Rail Overhead Contact Line Based on Wind Tunnel Tests. *IEEE Trans. Veh. Technol.* **2023**, *72*, 7211–7220. [CrossRef]
14. Zeng, J.D.; Li, M.S.; Li, Z.G.; Zhang, Z.T. Spatial correlation of along-wind fluctuating aerodynamic force acting on large aspect-ratio rectangular prisms. *J. Wind Eng. Ind. Aerodyn.* **2022**, *224*, 104951. [CrossRef]
15. Davenport, A.G. Gust loading factors. *J. Struct. Div. ASCE* **1967**, *93*, 11–34. [CrossRef]
16. Solari, G. Mathematical model to 3-D wind loading on buildings. *J. Eng. Mech. ASCE.* **1985**, *111*, 254–276. [CrossRef]
17. Kareem, A.; Zhou, Y. Gust loading factors—Past, present and future. *J. Wind Eng. Ind. Aerodyn.* **2003**, *91*, 1301–1328. [CrossRef]
18. Kwok, K.C.S. Cross-wind response of tall buildings. *Eng. Struct.* **1982**, *4*, 256–262. [CrossRef]
19. Lin, N.; Letchford, C.; Tamura, T.; Liang, B.; Nakamura, O. Characteristics of wind forces acting on tall buildings. *J. Wind Eng. Ind. Aerodyn.* **2005**, *93*, 217–242. [CrossRef]
20. Quan, Y.; Cao, H.L.; Gu, M. Effects of turbulence intensity and exterior geometry on across-wind aerodynamic damping of rectangular super-tall buildings. *Wind Struct.* **2016**, *22*, 185–209. [CrossRef]
21. Vickery, B.J.; Basu, R.I. Acrosswind vibrations of structures of circular corss-section. Part 1: Development of a mathematical model for two-dimensional conditions. *J. Wind Eng. Ind. Aerodyn.* **1983**, *12*, 49–73. [CrossRef]
22. Feng, C.; Chen, X. Estimation of Nonstationary Crosswind Response of Tall Buildings with Nonlinear Aeroelastic Effect. *J. Eng. Mech.* **2018**, *144*, 04018053. [CrossRef]
23. Cao, S.Y.; Zhou, Q.; Zhou, Z.Y. Velocity shear flow over rectangular cylinders with different side ratio. *Comp. Struct.* **2014**, *96*, 35–46. [CrossRef]
24. Architectural Institute of Japan (AIJ). *Recommendations for Loads on Building*; Architectural Institute of Japan: Tokyo, Japan, 2014.
25. Zeng, J.D.; Zhang, Z.T.; Li, M.S.; Li, S.P. Across-wind fluctuating aerodynamic force acting on large aspect-ratio rectangular prisms. *J. Fluids Struct.* **2023**, *121*, 103935. [CrossRef]
26. Liang, S.; Li, Q.S.; Liu, S.; Zhang, L.L.; Gu, M. Torsional dynamic wind loads on rectangular tall buildings. *Eng. Struct.* **2004**, *26*, 129–137. [CrossRef]
27. Yi, L.; Zhang, J.W.; Li, Q.S. Experimental investigation of characteristics of torsional wind loads on rectangular tall buildings. *Struct. Eng. Mech.* **2014**, *49*, 129–145. [CrossRef]
28. Braun, A.L.; Awruch, A.M. Aerodynamic and aeroelastic analyses on the CAARC standard tall building model using numerical simulation. *Comput. Struct.* **2009**, *87*, 564–581. [CrossRef]
29. Meng, F.Q.; He, B.J.; Zhu, J.; Zhao, D.X.; Zhao, Z.Q. Sensitivity analysis of wind pressure coefficients on CAARC standard tall buildings in CFD simulations. *J. Build. Eng.* **2018**, *16*, 146–158. [CrossRef]
30. Li, S.P.; Liu, Y.L.; Li, M.; Zeng, W.Y.; Gu, S.T.; Gao, Y. The effect of turbulence intensity on the unsteady gust loading on a 5:1 rectangular cylinder. *J. Wind Eng. Ind. Aerodyn.* **2022**, *225*, 104994. [CrossRef]
31. Svete, A.; Kutin, J. Identifying the high-frequency response of a piezoelectric pressure measurement system using a shock tube primary method. *Mech. Syst. Signal Process.* **2022**, *162*, 108014. [CrossRef]
32. *GB 50009-2012*; Load Code for the Design of Building Structures. Architectural Industry Press of China: Beijing, China, 2012.
33. Li, S.P.; Li, M.S.; Wu, B.; Li, K.; Yang, Y. Three-dimensional aerodynamic lift on a rectangular cylinder in turbulent flow at an angle of attack. *J. Fluids Struct.* **2023**, *118*, 103859. [CrossRef]
34. Li, Q.S.; Melbourne, W.J. The effect of large-scale turbulence on pressure fluctuations in separated and reattaching flows. *J. Wind Eng. Ind. Aerodyn.* **1999**, *83*, 159–169. [CrossRef]
35. Saathoff, P.J.; Melbourne, W.H. Effects of free stream turbulence on surface pressure fluctuations in a separation bubble. *J. Fluid Mech.* **1997**, *337*, 1–24. [CrossRef]
36. Xu, X.Y.; Li, Y.L.; Zhu, S.Y. Non-uniform wind excitation on dynamic responses of vehicle running on bridge. *J. Wind Eng. Ind. Aerodyn.* **2023**, *233*, 105301. [CrossRef]
37. Roy, K. Wind-uplift capacity of cold-formed steel weatherboard claddings—Experimental and numerical investigations. *Thin-Walled Struct.* **2023**, *184*, 110461. [CrossRef]
38. Roy, K. Wind-uplift capacity of cold-formed steel interlocking claddings-Experimental and numerical investigations. *J. Build. Eng.* **2023**, *63*, 105433. [CrossRef]